Satellite-clock modeling in single-frequency PPP-RTK processing

Wang, Kan; Khodabandeh, Amir; Teunissen, Peter J.G.; Nadarajah, Nandakumaran

DOI
10.1061/(ASCE)SU.1943-5428.0000252

Publication date
2018

Document Version
Final published version

Published in
Journal of Surveying Engineering

Satellite-Clock Modeling in Single-Frequency PPP-RTK Processing

Kan Wang[1]; Amir Khodabandeh[2]; Peter J. G. Teunissen[3]; and Nandakumaran Nadarajah[4]

Abstract: The real-time kinematic precise point positioning (PPP-RTK) technique enables integer ambiguity resolution by providing single-receiver users with information on the satellite phase biases next to the standard PPP corrections. Using undifferenced and uncombined observations, rank deficiencies existing in the design matrix need to be eliminated to form estimable parameters. In this contribution, the estimability of the parameters was studied in single-frequency ionosphere-weighted scenario, given a dynamic satellite-clock model in the network Kalman filter. In case of latency of the network corrections, the estimable satellite clocks, satellite phase biases, and ionospheric delays need to be predicted over short time spans. With and without satellite-clock models incorporated in the network Kalman filter, different approaches were used to predict the network corrections. This contribution shows how the predicted network corrections responded to the presence and absence of satellite-clock models. These differences in the predicted network corrections were also reflected in the user positioning results. Using three different 1-Hz global positioning system (GPS) single-frequency data sets, two user stations in one small-scale network were used to compute the positioning results, applying predicted network corrections. The latency of the network products ranges from 3 to 10 s. It was observed that applying strong satellite-clock constraints in the network Kalman filter (i.e., with the process noise of 1 or 0.5 mm per square root of second) reduced the root-mean squares (RMS) of the user positioning results to centimeters in the horizontal directions and decimeters in the vertical direction for latencies larger than 6 s, compared to the cases without a satellite-clock model. **DOI: 10.1061/(ASCE)SU.1943-5428.0000252.**

Author keywords: Single-frequency; Real-time kinematic precise point positioning (PPP-RTK); Satellite-clock modeling; Prediction.

Introduction

Using external information on satellite orbits and satellite clocks provided by, for example, the International Global Navigation Satellite System (GNSS) Service (IGS) (Dow et al. 2009), kinematic precise point positioning (PPP) results can nowadays reach centimeter-level accuracy (Yu and Gao 2017). However, to reach such an accuracy, long convergence time from tens of minutes to hours can be required (Banville et al. 2014; Leandro et al. 2011; Yu and Gao 2017). For single-frequency users, the precision of the kinematic PPP results by also applying external ionospheric information is normally at decimeter level (Huisman et al. 2012; van Bree and Tiberius 2012).

In network real-time kinematic (RTK) positioning, corrections are provided to the user in the *observation domain*. One can equivalently convey the information content in the network observations through physical parameters (e.g., satellite clocks, instrumental delays, and atmospheric biases). By using such *parameter-space* presentation, real-time kinematic precise point positioning (PPP-RTK) provides parameter corrections that have a lower sending rate, thus consuming a lower bandwidth for transmitting the corrections to the user (Wübbena et al. 2005). The PPP-RTK technique enables single-receiver integer ambiguity resolution (IAR) by giving users the satellite phase biases apart from the satellite orbits and the satellite clocks. In addition, the ionospheric delays, which are spatially interpolated for the user, can also be provided to speed up IAR (Odijk et al. 2014b). During the last 10 years, diverse studies have been performed to enable fast IAR and thus realize high-precision user positioning results in short time spans using dual-frequency and combined global positioning system (GPS) observations (Collins 2008; Ge et al. 2008; Geng et al. 2011; Laurichesse and Mercier 2007; Loyer et al. 2012; Teunissen et al. 2010). For a detailed review, see Teunissen and Khodabandeh (2015). For single-frequency PPP-RTK users, centimeter-level accuracy can also be reached for positioning within several minutes using undifferenced and uncombined observations, even with low-cost GNSS receivers (Odijk et al. 2012b). It was shown that single-frequency GPS + BeiDou navigation satellite system (BDS) RTK positioning with low-cost receivers can be competitive to dual-frequency GPS-only solutions using survey-grade receivers (Odolinski and Teunissen 2017). Using multi-GNSS signals, Li et al. (2017) proposed a new array-aided state-space RTK concept for single-frequency data processing, which improves the accuracy of the positioning results when increasing the number of the array antennas.

Using undifferenced and uncombined GPS L1 observations in PPP-RTK network processing, with the help of the *S*-system theory (Baarda 1981; Teunissen 1985), rank deficiencies of the design matrix are removed, leading to estimable combinations of the parameters (Odijk et al. 2012b). The estimable satellite clocks, satellite phase biases, and the interpolated user-specific ionospheric delays

[1]Research Associate, GNSS Research Centre, Curtin Univ., GPO Box U1987, Perth, WA 6845, Australia (corresponding author). ORCID: https://orcid.org/0000-0001-5688-6937. E-mail: kan.wang@curtin.edu.au

[2]Research Fellow, GNSS Research Centre, Curtin Univ., GPO Box U1987, Perth, WA 6845, Australia.

[3]Professor, GNSS Research Centre, Curtin Univ., GPO Box U1987, Perth, WA 6845, Australia; Professor, Dept. of Geoscience and Remote Sensing, Delft Univ. of Technology, PO Box 5048, 2600 GA, Delft, Netherlands.

[4]Research Fellow, GNSS Research Centre, Curtin Univ., GPO Box U1987, Perth, WA 6845, Australia.

Note. This manuscript was submitted on September 1, 2017; approved on December 21, 2017; published online on March 12, 2018. Discussion period open until August 12, 2018; separate discussions must be submitted for individual papers. This paper is part of the ***Journal of Surveying Engineering***, © ASCE, ISSN 0733-9453.

can then be provided to the user (Odijk et al. 2012b, 2014b). Because of the latencies of the PPP-RTK network products, the network corrections have to be predicted to bridge the time gap between the estimation of the network corrections and the user positioning. According to the study by Laurichesse et al. (2010), the overall latency of the network products based on a real-time integer PPP demonstrator developed by the Centre national d'études spatiales (CNES) is between 6 and 8 s. Leandro et al. (2011) also reported a total correction latency for the real-time extended (RTX) system (via a satellite link) of smaller than 5.6 s in 99% of the cases. To bridge the latency of the network products, a dynamic satellite-clock model can be incorporated into the network Kalman filter under a single-frequency scenario with the ionospheric delays spatially constrained between stations in a small-scale network [ionosphere-weighted model (Odijk 2002)]. Li et al. (2017) studied the estimability of the parameters without the satellite-clock model for a single-frequency scenario based on the assumption that the atmospheric delays are the same for all stations. In this contribution, with the help of *S*-system theory, the authors studied the estimability of the parameters, applying the satellite-clock model using undifferenced and uncombined observations under a single-frequency ionosphere-weighted scenario.

Using 1-Hz GPS single-frequency data from a small-scale network, estimated and predicted network corrections were studied and are discussed without and with clock constraints of different strengths. The influences of the satellite-clock models on the predicted network corrections lead to changes in the user positioning results. Using two user stations located within the network, based on the data of 3 different hours within 1 day, different sets of predicted network corrections were applied by the users. Without satellite-clock constraints, the satellite-clock estimates were predicted with the help of postcomputed satellite-clock rates, which can be obtained either by fitting polynomials using the satellite-clock estimates, or by directly setting to a constant value. With the satellite-clock model incorporated in the network Kalman filter, the satellite-clock rates were estimated in the Kalman filter and were used to predict the satellite clocks for different latencies. In this contribution, the influences of the predicted network corrections (with and without applying satellite-clock models) on the user positioning results were analyzed and are discussed with a latency ranging from 3 to 10 s using GPS L1 observations.

In the section "Processing Strategy," the authors first study the estimability of the network parameters without and with the satellite-clock models under a single-frequency and ionosphere-weighted scenario. A single-frequency network full-rank model applicable to an arbitrary GNSS was developed with a dynamic satellite-clock model incorporated into the network Kalman filter. The data selection and the impacts of the satellite-clock models on the estimated and the predicted network parameters are then discussed in the subsequent section. In the section "Latency and User Positioning Results," the influences of the satellite-clock modeling on the user positioning results are analyzed and discussed for latencies ranging from 3 to 10 s. The last section concludes this contribution.

Processing Strategy

For the single-frequency scenario, the observed-minus-computed (O-C) terms of the phase ($\Delta\phi^s_{r,j}$) and the code observations ($\Delta p^s_{r,j}$) can be formulated as follows (Hofmann-Wellenhof et al. 2008; Teunissen and Montenbruck 2017):

$$E\left(\Delta\phi^s_{r,j}\right) = g^s_r\tau_r + dt_r - dt^s - \mu_j\iota^s_r + \delta_{r,j} - \delta^s_{,j} + \lambda_j z^s_{r,j} \quad (1)$$

$$E\left(\Delta p^s_{r,j}\right) = g^s_r\tau_r + dt_r - dt^s + \mu_j\iota^s_r + d_{r,j} - d^s_{,j} \quad (2)$$

where the subindices r and j and the superindex s = receiver r (r = 1, …, n), frequency f_j, and satellite s (s = 1, …, m), respectively; and τ_r = zenith tropospheric delay (ZTD) for receiver r (after removing a priori values) with its mapping function (g^s_r) for receiver r and satellite s in front of it. In this study, the a priori ZTDs were modeled with the Saastamoinen model (Saastamoinen 1972) and were included in the O-C terms. dt_r and dt^s represent the receiver and the satellite clock, respectively, and ι^s_r stands for the ionospheric delay for receiver r and satellite s on a reference frequency (f_1) with coefficient $\mu_j = f_1^2/f_j^2$. The receiver and satellite hardware delays are denoted by $\delta_{r,j}$ and $\delta^s_{,j}$ for phase observations, and $d_{r,j}$ and $d^s_{,j}$ for code observations, respectively. The integer-valued ambiguity ($z^s_{r,j}$) is multiplied by the wavelength (λ_j). E (.) denotes the expectation operator.

Because the processing in this study was based on GPS L1 observations from a small-scaled network (with interstation distances within 50 km), weighted constraints were applied on the between-station ionospheric delays (Odijk 2002)

$$E\left(d\iota^s_{r\neq 1}\right) = \iota^s_{r\neq 1} - \iota^s_1 \quad (3)$$

where $d\iota^s_r$ (r = 2, …, n) = pseudo-observations having zero sample values with distance-dependent weights. The larger the between-station distances are, the smaller the weights become.

Using undifferenced and uncombined single-frequency GPS observations, as shown in Eqs. (1) and (2), singularities exist between the parameters. Based on the *S*-system theory (Baarda 1981; Teunissen 1985), the estimable parameters are formed by constraining a minimum set of *S*-basis parameters, so that the full-rank property of the design matrix can be recovered (Teunissen et al. 2010). The O-C terms of the phase and the code observations can be reformulated as

$$E\left(\Delta\phi^s_{r,j}\right) = g^s_r\tilde{\tau}_r + d\tilde{t}_r - d\tilde{t}^s - \mu_j\tilde{\iota}^s_r + \tilde{\delta}_{r,j} - \tilde{\delta}^s_{,j} + \lambda_j\tilde{z}^s_{r,j} \quad (4)$$

$$E\left(\Delta p^s_{r,j}\right) = g^s_r\tilde{\tau}_r + d\tilde{t}_r - d\tilde{t}^s + \mu_j\tilde{\iota}^s_r + \tilde{d}_{r,j} - \tilde{d}^s_{,j} \quad (5)$$

where the estimable parameters $\tilde{\tau}_r$, $d\tilde{t}_r$, $d\tilde{t}^s$, $\tilde{\iota}^s_r$, $\tilde{\delta}_{r,j}$, $\tilde{\delta}^s_{,j}$, $\tilde{d}_{r,j}$, $\tilde{d}^s_{,j}$, and $\tilde{z}^s_{r,j}$ are shown in Fig. 1. From Fig. 1, it can be seen that the ZTDs were estimated relatively based on the assumption that the ZTD mapping functions between stations in a small-scaled network were similar to each other ($g^s_{r\neq 1} \approx g^s_1$).

The estimable parameters (Fig. 1) were estimated in a Kalman filter in the Curtin PPP-RTK network software (Odijk et al. 2017). The ionospheric delays, the receiver and satellite hardware biases, and the ZTDs were linked in time with a random-walk process. The vector of the time-updated parameters ($\hat{x}_{i|i-1}$) and the corresponding variance–covariance matrix ($Q_{i|i-1}$) at epoch i were calculated based on the estimation of the last epoch (i.e., epoch $i-1$)

$$\hat{x}_{i|i-1} = \Phi_{i|i-1}\hat{x}_{i-1|i-1}, \quad Q_{i|i-1} = \Phi_{i|i-1}Q_{i-1|i-1}\Phi^T_{i|i-1} + S_{x_i} \quad (6)$$

where $\hat{x}_{i-1|i-1}$ and $Q_{i-1|i-1}$ = filtered parameters and the corresponding variance–covariance matrix at epoch $i-1$, respectively. The transition matrix ($\Phi_{i|i-1}$) time-predicts $\hat{x}_{i|i-1}$ from epoch $i-1$.

J. Surv. Eng., 2018, 144(2): 04018003

S_{x_i} represents the variance–covariance matrix of the system noise at epoch i.

Instead of estimating the satellite-clock parameters as time-unlinked parameters, as shown in Fig. 1, dynamic models can be applied to constrain the temporal behaviors of the satellite clocks. As described by Wang et al. (2017), the satellite-clock parameters can be modeled with the help of the satellite-clock rate ($\dot{dt}^s$)

$$\begin{bmatrix} dt^s(t_i) \\ \dot{dt}^s(t_i) \end{bmatrix} = \Phi^s_{i|i-1} \begin{bmatrix} dt^s(t_{i-1}) \\ \dot{dt}^s(t_{i-1}) \end{bmatrix} + \begin{bmatrix} \epsilon^s(t_i) \\ \dot{\epsilon}^s(t_i) \end{bmatrix} \tag{7}$$

with

$$\Phi^s_{i|i-1} = \begin{bmatrix} 1 & \Delta t_i \\ 0 & 1 \end{bmatrix}, \quad \Delta t_i = t_i - t_{i-1} \tag{8}$$

where ϵ^s and $\dot{\epsilon}^s$ = system noise of the satellite clock and the satellite-clock rate for satellite s, respectively.

Based on the study by Senior et al. (2008), different generations and types of the GPS satellite clocks may show different noise behaviors for different averaging times. To not increase the complexity and computational load for real-time usage (Hauschild and Montenbruck 2009), in this study, the authors did not attempt to distinguish the noise types between different GPS satellite clocks. The white frequency noise (WFN) was assumed to be the dominant noise type (Wang et al. 2017), and the two-state (clock and clock rate) variance matrix for WFN in the Kalman filter [i.e., the variance matrix for the terms ϵ^s and $\dot{\epsilon}^s$ in Eq. (7)] was formulated as follows (van Dierendonck et al. 1984):

Parameter	Interpretation
$\tilde{\tau}_{r\neq1}(t_1)$	$\tau_r(t_1) - \tau_1(t_1)$
$\tilde{\tau}_r(t_{i>1})$	$\tau_r(t_i) - \tau_1(t_1)$
$\tilde{dt}_{r\neq1}(t_i)$	$dt_{1r}(t_i) + d_{1r,j}(t_1)$
$\tilde{dt}^s(t_i)$	$dt^s(t_i) + d^s_{,j}(t_1) - (dt_1(t_i) + d_{1,j}(t_1)) - g^s_1(t_i)\tau_1(t_1) - \mu_j \iota^s_1(t_1)$
$\tilde{\iota}^s_r(t_i)$	$\iota^s_r(t_i) - \iota^s_1(t_1), \begin{cases} r \neq 1, i = 1 \\ \forall r, i > 1 \end{cases}$
$\tilde{\delta}_{r,j}(t_i)$	$\delta_{r,j}(t_i) - \delta_{1,j}(t_1) - d_{1r,j}(t_1) + z^1_{1r,j}\lambda_j, \begin{cases} r \neq 1, i = 1 \\ \forall r, i > 1 \end{cases}$
$\tilde{\delta}^s_j(t_i)$	$\delta^s_j(t_i) - \delta_{1,j}(t_1) - (d^s_{,j}(t_1) - d_{1,j}(t_1)) + 2\mu_j \iota^s_1(t_1) - z^s_{1,j}\lambda_j$
$\tilde{d}_{r,j}(t_{i>1})$	$d_{r,j}(t_i) - d_{r,j}(t_1)$
$\tilde{d}^s_j(t_{i>1})$	$d^s_{,j}(t_i) - d^s_{,j}(t_1)$
$\tilde{z}^{s\neq1}_{r\neq1,j}$	$z^s_{1r,j} - z^1_{1r,j}$
S-basis	$\tau_1(t_1), dt_1(t_i), \delta_{1,j}(t_1), d_{r,j}(t_1), d^s_{,j}(t_1), \iota^s_1(t_1), z^s_{1,j}, z^1_{r,j}$

Fig. 1. Estimable parameters and *S*-basis parameters in Eqs. (4) and (5) with the ionospheric delays, the hardware biases, and the ZTDs linked in time (as random-walk process) for a *single*-frequency ionosphere-weighted scenario *without* satellite-clock model; *relative* ZTDs between stations are estimated

$$S_{\dot{dt}^s}(t_i) = \begin{bmatrix} \frac{h_0}{2}\Delta t_i & 0 \\ 0 & \frac{h_0}{2\Delta t_i} \end{bmatrix} \cdot c^2 = q^2_{\dot{dt}^s} \begin{bmatrix} \frac{\Delta t_i}{2} & 0 \\ 0 & \frac{1}{2\Delta t_i} \end{bmatrix} \tag{9}$$

with

$$h_0 = \sigma^2_A \cdot 2\tau, \quad q_{\dot{dt}^s} = \sqrt{h_0} \cdot c \tag{10}$$

where c = speed of light; and σ_A and τ = Allan deviation (Allan 1987) and the corresponding averaging time, respectively. For WFN, with a slope of –0.5 in the sigma-tau diagram of the Allan deviations (Riley 2008), the parameter $q_{\dot{dt}^s}$ is a constant value.

Applying the satellite-clock model [Eq. (7)], the estimability of the receiver and satellite clocks changed, and the ZTDs could be estimated absolutely for each station. The changes in the estimable parameters (compared to those shown in Fig. 1) are shown in Fig. 2. Compared to the case with unlinked satellite clocks (Fig. 1), the reference receiver clocks at the third epoch (and beyond) [i.e., $dt_1(t_{i>2})$] were not constrained as *S*-basis parameters anymore.

Based on Figs. 1 and 2, the number of the observation equations (including the constraint equations, denoted as l_o), the number of the estimable parameters (l_u), and the number of the redundancies (l_r) are shown in Fig. 3 for the cases without a satellite-clock model. The addition of the numbers after applying the satellite-clock model is marked for satellite clocks/rates in l_o; for ZTDs, receiver clocks, and satellite clocks/rates in l_u; and for redundancy in l_r. t_1 and t_2 represent the first and second time epochs of the processing, respectively, and $t_{i>1}$ and $t_{i>2}$ represent the time after the first and second epochs, respectively. n and m represent the number of receivers and satellites at the corresponding epoch, respectively. Based on Eqs. (4) and (5), $2nm$ phase and code measurements were received by the receivers. In addition, the ionosphere-weighted model [Eq. (3)] provided $(n-1)m$ constraint equations. From the second epoch (t_2, without a satellite-clock model), with the time links of the ZTDs (n), the receiver hardware biases ($2n$), the satellite hardware biases ($2m$), the ionospheric delays (nm), and the ambiguities [$(n-1)(m-1)$], $2mn+m+2n+1$ additional time-constraint equations were available. With a satellite-clock model, m more constraint equations were available for $t_{i>2}$ for the satellite clocks and the satellite-clock rates, respectively. This led to an addition of l_o of $2m$. Based on Fig. 1, without a satellite-clock model, $2nm+2n-2$ and $2nm+3n+2m$ estimable parameters need to be estimated at the first epoch and for $t_{i>1}$, respectively. Applying a satellite-clock model made the estimation of the absolute ZTDs possible (Fig. 2). This led to one more estimable parameter at t_1. For $t_{i>2}$, m estimable satellite-clock rates and the estimable reference receiver clock were also added to l_u. This led to the addition of $m+1$ for l_u in total for $t_{i>2}$. As a result, from the box for l_r in Fig. 3, it can be seen that the redundancy at t_1 decreased by 1 when applying a satellite-clock model due to the change from relative to absolute ZTD estimation

Parameter	Interpretation
$\tilde{\tilde{\tau}}_r(t_i)$	$\tau_r(t_i)$
$\tilde{\tilde{dt}}_r(t_i)$	$dt_r(t_i) + d_{1r,j}(t_1) - dt_1(t_1) - \frac{t_i - t_1}{\Delta t_2}(dt_1(t_2) - dt_1(t_1)), \begin{cases} r \neq 1, i = 1, 2 \\ \forall r, i > 2 \end{cases}$
$\tilde{\tilde{dt}}^s(t_i)$	$dt^s(t_i) + d^s_{,j}(t_1) - (dt_1(t_1) + d_{1,j}(t_1)) - \mu_j \iota^s_1(t_1) - \frac{t_i - t_1}{\Delta t_2}(dt_1(t_2) - dt_1(t_1))$
$\dot{\tilde{\tilde{dt}}}^s(t_{i>2})$	$\dot{dt}^s(t_i) - \frac{1}{\Delta t_2}(dt_1(t_2) - dt_1(t_1))$

Fig. 2. Changed estimable parameters *with* the satellite-clock model [Eq. (7)] with the ionospheric delays, the hardware biases, and the ZTDs linked in time (as random-walk process) for a *single*-frequency ionosphere-weighted scenario; *absolute* ZTDs are estimated for each station

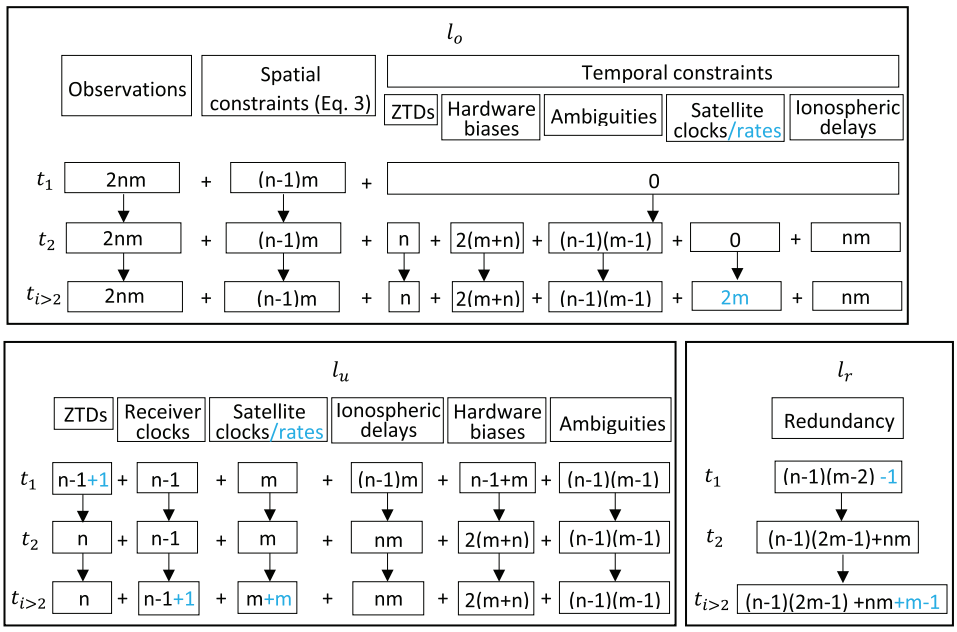

Fig. 3. Flowcharts of the number of observation equations (including the constraint equations, denoted as l_o), number of estimable parameters (l_u), and number of redundancies (l_r) without satellite-clock model, and the addition of numbers after applying the satellite-clock model (see Figs. 1 and 2)

(with an additional parameter). However, for $t_{i>2}$, the redundancy l_r increased by $m-1$ after applying the satellite-clock model.

With Fig. 2 and Eq. (7), the following equations can be obtained:

$$\begin{aligned} &d\tilde{t}^s(t_i) = dt^s(t_i) + d^s_{,j}(t_1) - [dt_1(t_1) + d_{1,j}(t_1)] - \mu_j \iota^s_1(t_1) \\ &-\frac{t_i - t_1}{\Delta t_2}[dt_1(t_2) - dt_1(t_1)] = dt^s(t_{i-1}) + \Delta t_i \dot{dt}^s(t_{i-1}) + \epsilon^s(t_i) \\ &+ d^s_{,j}(t_1) - [dt_1(t_1) + d_{1,j}(t_1)] - \mu_j \iota^s_1(t_1) - \left(\frac{t_{i-1} - t_1}{\Delta t_2} + \frac{\Delta t_i}{\Delta t_2}\right) \\ &\times [dt_1(t_2) - dt_1(t_1)] = d\tilde{t}^s(t_{i-1}) + \Delta t_i \dot{d\tilde{t}}^s(t_{i-1}) + \epsilon^s(t_i) \end{aligned} \tag{11}$$

$$\begin{aligned} \dot{d\tilde{t}}^s(t_i) &= \dot{dt}^s(t_i) - \frac{1}{\Delta t_2}[dt_1(t_2) - dt_1(t_1)], \\ &= \dot{dt}^s(t_{i-1}) + \dot{\epsilon}^s(t_i) - \frac{1}{\Delta t_2}[dt_1(t_2) - dt_1(t_1)], \\ &= \dot{d\tilde{t}}^s(t_{i-1}) + \dot{\epsilon}^s(t_i) \end{aligned} \tag{12}$$

From Eqs. (11) and (12), it can be seen that the satellite-clock model [Eq. (7)] also applies to the new *estimable* satellite clocks ($d\tilde{t}^s$) and satellite-clock rates ($\dot{d\tilde{t}}^s$)

$$\begin{bmatrix} d\tilde{t}^s(t_i) \\ \dot{d\tilde{t}}^s(t_i) \end{bmatrix} = \Phi^s_{i|i-1} \begin{bmatrix} d\tilde{t}^s(t_{i-1}) \\ \dot{d\tilde{t}}^s(t_{i-1}) \end{bmatrix} + \begin{bmatrix} \epsilon^s(t_i) \\ \dot{\epsilon}^s(t_i) \end{bmatrix} \tag{13}$$

With the estimable satellite clocks ($d\tilde{t}^s$, without clock model), satellite phase biases ($\tilde{\delta}^s_{,j}$), and network-derived user ionospheric delays ($\tilde{\iota}^s_u$) (Wang et al. 2017) provided to the users, the O-C terms of the phase and the code observations at the user side can be formulated as follows:

$$E(\Delta\phi^s_{u,j}) + d\tilde{t}^s + \tilde{\delta}^s_{,j} + \mu_j \tilde{\iota}^s_u = \Delta\tilde{\rho}^s_u + d\tilde{t}_u + \tilde{\delta}_{u,j} + \lambda_j \tilde{z}^s_{u,j} \tag{14}$$

$$E(\Delta p^s_{u,j}) + d\tilde{t}^s - \mu_j \tilde{\iota}^s_u = \Delta\tilde{\rho}^s_u + d\tilde{t}_u + \tilde{d}_{u,j} - \tilde{d}^s_{,j} \tag{15}$$

where the term $\Delta\tilde{\rho}^s_u$ contains the increment of the user station coordinates and the *relative* user ZTD (Fig. 1) in the slant direction. If the satellite-clock models are applied, the estimable satellite clocks ($d\tilde{t}^s$) in Eqs. (14) and (15) are replaced by those applying the satellite-clock model ($d\tilde{\tilde{t}}^s$) instead

$$E(\Delta\phi^s_{u,j}) + d\tilde{\tilde{t}}^s + \tilde{\delta}^s_{,j} + \mu_j \tilde{\iota}^s_u = \Delta\tilde{\tilde{\rho}}^s_u + d\tilde{\tilde{t}}_u + \tilde{\delta}_{u,j} + \lambda_j \tilde{z}^s_{u,j} \tag{16}$$

$$E(\Delta p^s_{u,j}) + d\tilde{\tilde{t}}^s - \mu_j \tilde{\iota}^s_u = \Delta\tilde{\tilde{\rho}}^s_u + d\tilde{\tilde{t}}_u + \tilde{d}_{u,j} - \tilde{d}^s_{,j} \tag{17}$$

where the term $\Delta\tilde{\tilde{\rho}}^s_u$ contains the increment of the user station coordinate and the *absolute* user ZTD (Fig. 2) in the slant direction. $d\tilde{\tilde{t}}_u$ represents the estimable user receiver clock with the form in Fig. 2.

For the network and the user processing, the a priori standard deviations at the zenith direction were set to be 3 mm (σ_ϕ) and 3 dm (σ_p) for the phase and the code observations, respectively. Given these a priori standard deviations, elevation-dependent weighting function (Eueler and Goad 1991) can be applied to the observations with the following (Dach et al. 2007):

$$w_\phi(e) = \frac{\sin^2(e)}{\sigma^2_\phi} \tag{18}$$

$$w_p(e) = \frac{\sin^2(e)}{\sigma^2_p} \tag{19}$$

where e = elevation angle of the observation; and $w_\phi(e)$ and $w_p(e)$ = elevation-dependent weights of the phase and the code observations, respectively. During the network processing, the ultrarapid satellite orbits provided by the IGS with predicted satellite positions (Dow et al. 2009; Springer and Hugentobler 2001) and the precise station coordinates provided by Geoscience Australia (GA) (GA 2017) were used for generating the O-C terms and were not

estimated. As shown in Table 1, the ZTDs, hardware biases, and ionospheric delays were linked in time. The ambiguities were assumed to be constant, and the satellite clocks were estimated for both cases as unlinked and linked parameters. The spatial ionosphere-weighted model was applied with the standard deviation of the between-station single-differenced ionospheric delays set as 0.03 m per 20 km. The partial IAR (Odijk et al. 2014a) with a predefined ambiguity success rate of 99.99% was used in both the network and the user processing.

Network Corrections without and with Satellite-Clock Modeling

In the processing, the authors used 1-Hz GPS L1 data from a small-scale network located in Victoria, Australia (Fig. 4) on March 28, 2017 from 5:00 to 7:00, from 13:00 to 15:00, and from 21:00 to 23:00 in GPS Time (GPST). The network consisted of four stations (see the stations DORA, KEPK, WBEE and CLYT in Fig. 4) with an interstation distance ranging from 19.6 to 42.9 km. Two stations were used as the user stations (see the stations PKVL and MOBS in Fig. 4). The network stations all used Trimble (Sunnyvale, California) NetR9 receivers, and the two user stations used Leica (St. Gallen, Switzerland) GRX1200GGPRO and Septentrio (Leuven, Belgium) POLARX4 receivers, respectively. Because the network products were assumed to be provided to the users over a long time period, the user processing started 1 h after the network processing. For newly risen satellites during the user processing, the network products of the first 8 min were considered within the initialization phase of the network Kalman filter and were not used by the user. The elevation mask was set to 10°. In this study, the GPS L1 observations were used for the network and the user processing. However, it is noted that the estimability of the parameters introduced in the previous section also applied for single-frequency signals of other GNSS or multi-GNSS single-frequency signals. When processing multi-GNSS single-frequency observations, the intersystem biases (ISBs) need to be properly considered (Odijk et al. 2012a).

Table 1. Settings of Dynamic Model in Network Kalman Filter

Parameter	Process noise
Receiver hardware delays ($m/\sqrt{s}$)	1
Satellite hardware delays ($m/\sqrt{s}$)	0.01
ZTDs ($mm/\sqrt{s}$)	0.1
Ionospheric delays ($m/\sqrt{s}$)	0.5
Satellite clocks ($mm/\sqrt{s}$)	Unlinked, 7, 1, 0.5
Ambiguities ($m/\sqrt{s}$)	0

Note: Parameters not listed in this table are estimated as unlinked parameters.

As shown by Khodabandeh and Teunissen (2015), the between-satellite differences in the network corrections take an active role in user positioning. As a result, for the user positioning, the network products are effective or largely effective at the between-satellite level, if the receiver clocks and hardware biases are unlinked or very weakly linked in time. Based on Figs. 1 and 2, the between-satellite clocks without ($d\tilde{t}^{1s}$) and with the satellite-clock models ($d\tilde{\tilde{t}}^{1s}$) have the following formulation:

$$d\tilde{t}^{1s}(t_i) = dt^{1s}(t_i) + d^{1s}_{,j}(t_1) - \mu_j \iota^{1s}_1(t_1) - g^{1s}_1(t_i)\tau_1(t_1) \tag{20}$$

$$d\tilde{\tilde{t}}^{1s}(t_i) = dt^{1s}(t_i) + d^{1s}_{,j}(t_1) - \mu_j \iota^{1s}_1(t_1) \tag{21}$$

The difference between $d\tilde{\tilde{t}}^{1s}$ and $d\tilde{t}^{1s}$ at the time point t_i is thus the term $g^{1s}_1(t_i)\tau_1(t_1)$. $\tau_1(t_1)$ can be obtained by

$$\tau_1(t_1) = \frac{d\tilde{\tilde{t}}^{1s}(t_i) - d\tilde{t}^{1s}(t_i)}{g^{1s}_1(t_i)} \tag{22}$$

As examples, Fig. 5(a) shows the between-satellite differences of the ZTD mapping functions (g^{1s}_1) for the satellite pairs G07-G09, G07-G30, G07-G23, G07-G27, and the $\tau_1(t_1)$ obtained from Eq. (22) using the between-satellite-clock estimates $d\hat{t}^{1s}$ without a satellite-clock model and $d\hat{\hat{t}}^{1s}$ with a satellite-clock model

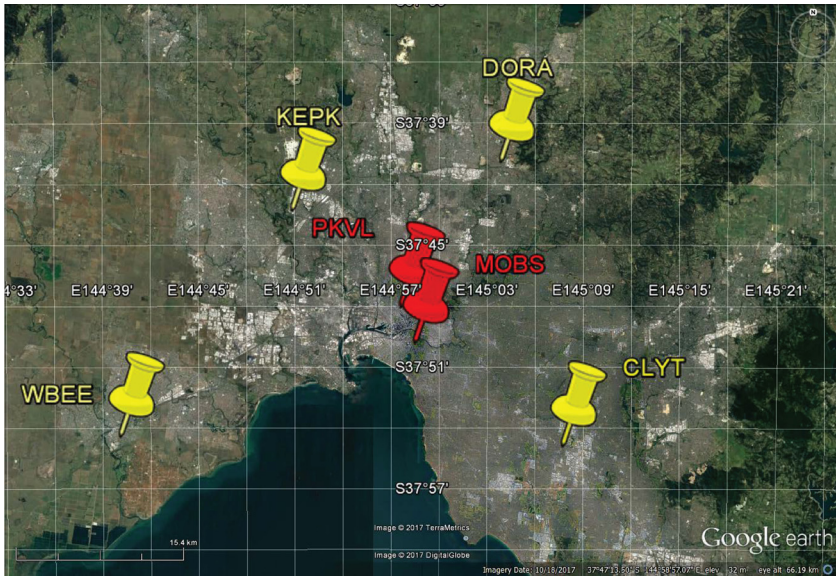

Fig. 4. Local network for the network and user processing on March 28, 2017; Stations PKVL and MOBS are used as user stations and the other stations are used as network stations; interstation distance of the network stations ranges from 19.6 to 42.9 km (Map data @ 2017 Google, Image © 2017 TerraMetrics, Image © 2017 DigitalGlobe) (Google Earth 2017)

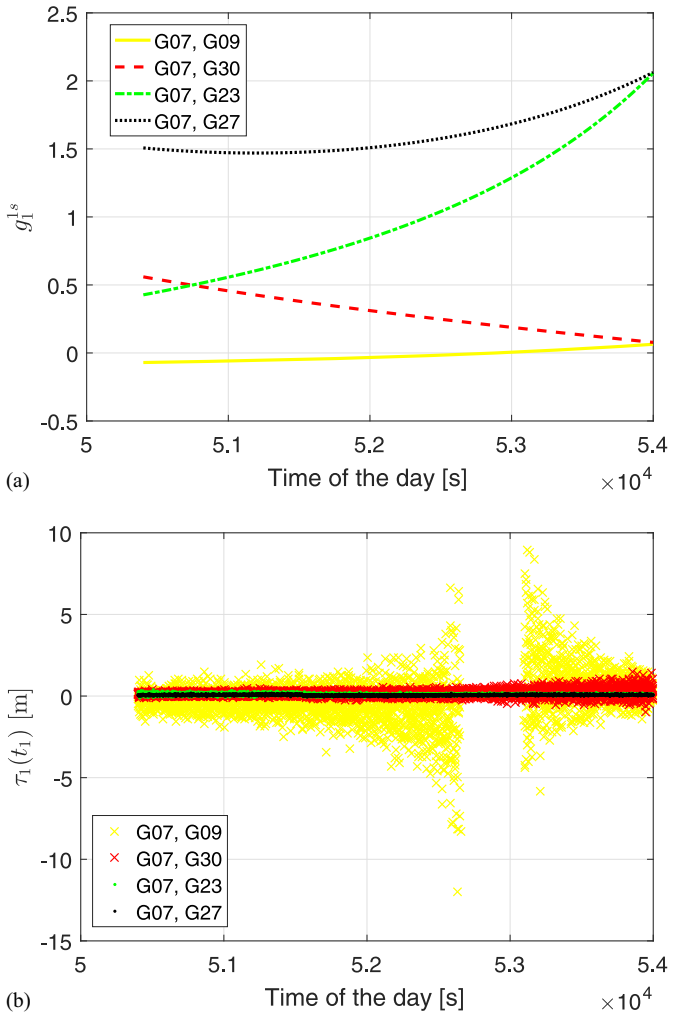

Fig. 5. (a) Between-satellite differences of the mapping functions for ZTDs and (b) $\tau_1(t_1)$ obtained with Eq. (22) for the satellite pairs G07-G09, G07-G30, G07-G23, and G07-G27 from 14:00 to 15:00 on March 28, 2017; the reference station (Station 1) is Station DORA (see Fig. 4)

($q_{dt^s} = 7$ mm/$\sqrt{\text{s}}$) from 14:00 to 15:00 on March 28, 2017. The signals of these satellites were received by all network stations from the start of the network processing, and the *S*-basis parameters $\iota_1^s(t_1)$ and $\tau_1(t_1)$ (Figs. 1 and 2) for these satellites related to the same reference receiver. The time intervals with g_1^{1s} near zero (with an absolute value smaller than 0.01) were excluded from Fig. 5(b) for the purpose of visualization. Fig. 5(b) shows that the variance of $\tau_1(t_1)$ increased with the decreasing absolute value of g_1^{1s}. Using the data from the satellite pair G07-G27 with relatively large absolute g_1^{1s} and small changes in the variance of $\tau_1(t_1)$, the mean value of $\tau_1(t_1)$ amounted to approximately 6 cm.

Fig. 6 shows the formal standard deviations of the estimable between-satellite clocks without and with clock constraint for Satellites G07 and G09 from 14:00 to 15:00 on March 28, 2017. To test the influences of the satellite-clock constraints with different strengths on the results, the values 7, 1, and 0.5 mm/$\sqrt{\text{s}}$ were used for the parameter q_{dt^s} [Eq. (10)] with decreasing system noise. Fig. 6 shows that the formal standard deviations of the estimable between-satellite clocks for G07 and G09 from 14:00 to 15:00 amounted to several decimeters. Applying a satellite-clock model

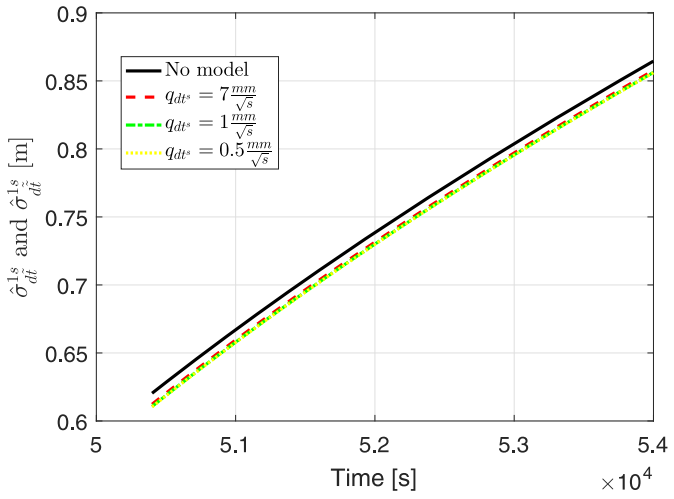

Fig. 6. Formal standard deviations of the estimable between-satellite clocks without and with satellite-clock model for Satellites G07 and G09 from 14:00 to 15:00 (in GPST) on March 28, 2017

helped to reduce the formal standard deviations by millimeters (up to centimeters), and thus improved the precision of the between-satellite-clock estimates.

The between-satellite single-frequency combined network corrections without a satellite-clock model ($\tilde{\omega}_{r,j}^{1s}$) and with a satellite-clock model ($\tilde{\tilde{\omega}}_{r,j}^{1s}$) are defined as follows (see also Figs. 1 and 2):

$$\begin{aligned}\tilde{\omega}_{r,j}^{1s}(t_i) &= d\tilde{t}^{1s}(t_i) + \tilde{\delta}_{,j}^{1s}(t_i) + \mu_j \tilde{\iota}_r^{1s}(t_i) \\ &= dt^{1s}(t_i) + \delta_{,j}^{1s}(t_i) + \mu_j \iota_r^{1s}(t_i) - g_1^{1s}(t_i)\tau_1(t_1) - z_{1,j}^{1s}\lambda_j\end{aligned} \tag{23}$$

$$\begin{aligned}\tilde{\tilde{\omega}}_{r,j}^{1s}(t_i) &= d\tilde{\tilde{t}}^{1s}(t_i) + \tilde{\delta}_{,j}^{1s}(t_i) + \mu_j \tilde{\iota}_r^{1s}(t_i) \\ &= dt^{1s}(t_i) + \delta_{,j}^{1s}(t_i) + \mu_j \iota_r^{1s}(t_i) - z_{1,j}^{1s}\lambda_j\end{aligned} \tag{24}$$

As an example, Fig. 7(a) shows the formal standard deviations of the between-satellite combined network correction $\hat{\sigma}_{\tilde{\omega}_{r,j}^{1s}}$ (without satellite-clock model) and $\hat{\sigma}_{\tilde{\tilde{\omega}}_{r,j}^{1s}}$ (with satellite-clock model) between Satellites G07 and G09 for the network Station WBEE from 14:00 to 15:00 on March 28, 2017. Fig. 7(a) shows that the decimeter-level formal standard deviations visible in Fig. 6 were significantly reduced when combining the network corrections. The differences in the formal standard deviations without and with satellite-clock models for G07 and G09 from 14:00 to 15:00 were smaller than submillimeter.

The different formal standard deviations of the single and combined network products were caused by the strong correlation among the between-satellite clocks ($d\tilde{t}^{1s}$ without clock model or $d\tilde{\tilde{t}}^{1s}$ with clock model), the between-satellite ionospheric delays ($\tilde{\iota}_r^{1s}$), and the between-satellite phase biases ($\tilde{\delta}_{,j}^{1s}$). Fig. 7(b) shows, for example, the correlation coefficients of the between-satellite clocks and the sum of the between-satellite ionospheric delays (for the Network Station WBEE) and the between-satellite phase biases from 14:00 to 15:00 on March 28, 2017 for the satellite pair G07 and G09, which is formulated as

$$\tilde{\varphi}_{r,j}^{1s} = \tilde{\delta}_{,j}^{1s} + \mu_j \tilde{\iota}_r^{1s} \tag{25}$$

Fig. 7(b) shows that the absolute values of the correlation coefficients between $d\tilde{t}^{1s}$ without a satellite-clock model (or $d\tilde{\tilde{t}}^{1s}$ with a

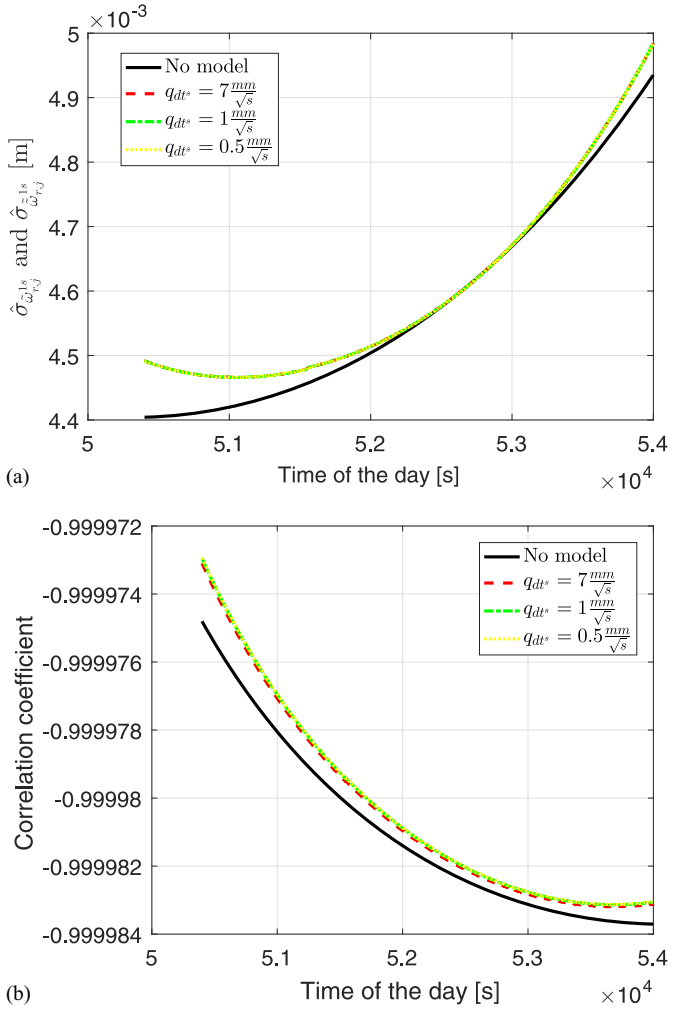

Fig. 7. (a) Formal standard deviations of the between-satellite combined network corrections [Eqs. (23) and (24)] for the network Station WBEE without ($\hat{\sigma}_{\tilde{\omega}^{1s}_{r,j}}$) and with satellite-clock models ($\hat{\sigma}_{\tilde{\tilde{\omega}}^{1s}_{r,j}}$); (b) correlation coefficients between $d\tilde{t}^{1s}$ (or $d\tilde{\tilde{t}}^{1s}$) and $\tilde{\varphi}^{1s}_{r,j}$ [for the network Station WBEE, see Eq. (25)] for Satellites G07 and G09 from 14:00 to 15:00 on March 28, 2017

satellite-clock model) and $\tilde{\varphi}^{1s}_{r,j}$ were large, which indicates a strong correlation among the network corrections. Applying satellite-clock models slightly reduced the absolute values of the correlation coefficients. The reduced formal standard deviations of the between-satellite combined network corrections [Fig. 7(a)] compared to those of the between-satellite clocks (Fig. 6) can be explained by the high correlations shown in Fig. 7(b) (Khodabandeh and Teunissen 2015). Accordingly, although the precision of each individual between-satellite correction (satellite clocks, satellite phase biases, and ionospheric delays) was driven by the code data, the precision of their combined version was at the phase level.

According to Bevis et al. (1992) and Younes (2016), the wet component of ZTDs can vary from centimeters (or less) in arid regions to as large as 35 cm in humid regions. With g^{1s}_1 for the satellite pairs G07 and G09 (from 14:00 to 15:00 on March 28, 2017) shown in Fig. 5(a) varying from approximately –0.07 to 0.06, the term $g^{1s}_1(t_i)\tau_1(t_1)$ for G07 and G09 during this time interval thus generally varied from submillimeters to millimeters, and did not exceed 2.5 cm in the extreme cases (i.e., with the wet component increment of ZTD for the reference receiver at t_1 amounting to 35 cm). Based on the small differences of $\tilde{\omega}^{1s}_{r,j}$ and $\tilde{\tilde{\omega}}^{1s}_{r,j}$ for this satellite pair and test interval per definition [Eqs. (23) and (24)], the estimates of the between-satellite combined network corrections for Station WBEE without a satellite-clock model ($\hat{\tilde{\omega}}^{1s}_{r,j}$) and with a satellite-clock model ($\hat{\tilde{\tilde{\omega}}}^{1s}_{r,j}$) were compared. For a better visualization, the between-satellite-clock drift and offset derived from the IGS clock biases (IGS Clock 2017) for G07 and G09 from 14:00 to 15:00 on March 28, 2017 were subtracted from the between-satellite combined network corrections to generate the residuals

$$\Delta\hat{\tilde{\omega}}^{1s}_{r,j}(t_i) = \hat{\tilde{\omega}}^{1s}_{r,j}(t_i) - \hat{p}^{1s}_1 \cdot (t_i - t_0) - \hat{p}^{1s}_0 \tag{26}$$

$$\Delta\hat{\tilde{\tilde{\omega}}}^{1s}_{r,j}(t_i) = \hat{\tilde{\tilde{\omega}}}^{1s}_{r,j}(t_i) - \hat{p}^{1s}_1 \cdot (t_i - t_0) - \hat{p}^{1s}_0 \tag{27}$$

where the satellite-clock rate ($\hat{p}^s_1$) and offset ($\hat{p}^s_0$) are derived from the IGS satellite-clock biases ($\hat{dt}^s_{\mathrm{IGS}}$) with

$$\hat{dt}^s_{\mathrm{IGS}}(t_i) = p^s_1(t_i - t_0) + p^s_0 \tag{28}$$

where t_0 = 14:00 on March 28, 2017.

Fig. 8(a) shows the residuals of the between-satellite combined network corrections without and with satellite-clock models [Eqs. (26) and (27)] for Station WBEE for G07 and G09 from 14:00 to 15:00 on March 28, 2017. It can be seen that the results are almost overwritten by each other (with differences within millimeters). Based on Eqs. (23) and (24), the variation of $\Delta\hat{\tilde{\omega}}^{1s}_{r,j}$ and $\Delta\hat{\tilde{\tilde{\omega}}}^{1s}_{r,j}$ should be related to the stochastic behaviors of the satellite clocks (after removing offset and drift) on a between-satellite level, possible cycle slips in $z^{1s}_{1,j}$, the variation of the between-satellite phase biases, the between-satellite ionospheric biases, and the term $g^{1s}_1(t_i)\tau_1(t_1)$ (for relative ZTD estimation). After adding the between-satellite O-C term of the phase observations for Station WBEE [$\Delta\phi^{1s}_{r,j}$, see Eq. (4)] to its between-satellite combined network corrections from 14:00 to 15:00 on March 28, 2017, the short-term variation in Fig. 8(a) at decimeter level was reduced to millimeter level [see Fig. 8(b)]. The expectation of the remaining parts of $\Delta\phi^{1s}_{r,j} + \hat{\tilde{\omega}}^{1s}_{r,j}$ (without satellite-clock model) and $\Delta\phi^{1s}_{r,j} + \hat{\tilde{\tilde{\omega}}}^{1s}_{r,j}$ (with satellite-clock model) contain the term of the tropospheric delays ($g^{1s}_r\tilde{\tau}_r$ and $g^{1s}_r\tilde{\tilde{\tau}}_r$) and the ambiguities

$$E\left(\Delta\tilde{\phi}^{1s}_{r,j}\right) = E\left(\Delta\phi^{1s}_{r,j} + \hat{\tilde{\omega}}^{1s}_{r,j}\right) = g^{1s}_r\tilde{\tau}_r + \lambda_j\tilde{z}^{1s}_{r,j} \tag{29}$$

$$E\left(\Delta\tilde{\tilde{\phi}}^{1s}_{r,j}\right) = E\left(\Delta\phi^{1s}_{r,j} + \hat{\tilde{\tilde{\omega}}}^{1s}_{r,j}\right) = g^{1s}_r\tilde{\tilde{\tau}}_r + \lambda_j\tilde{z}^{1s}_{r,j} \tag{30}$$

Therefore, the conclusion is that applying a satellite-clock model does not generate significant differences in the between-satellite combined network corrections compared to the case without a satellite-clock model. However, the situation changes in the case of latencies (i.e., when the network corrections need to be *predicted*).

In the case of latencies, the network corrections were predicted separately for each parameter (the estimable satellite clocks, satellite phase biases, and user-specific ionospheric delays). Corresponding to the settings in the network Kalman filter, the estimable satellite phase biases and user-specific ionospheric delays at the

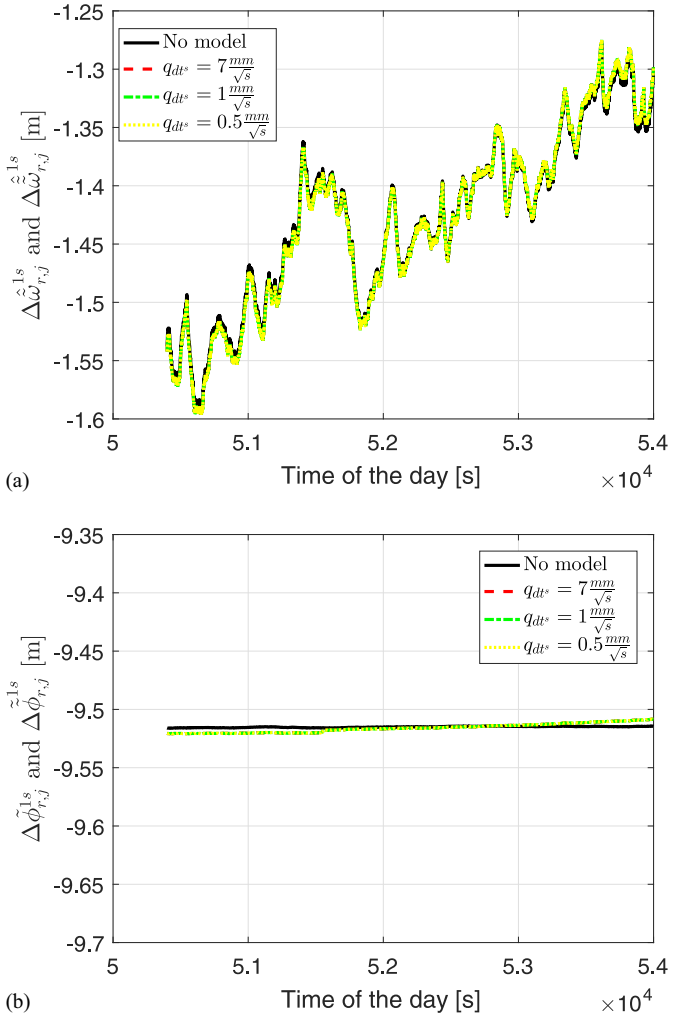

Fig. 8. (a) Residual between-satellite combined network corrections [$\Delta\hat{\tilde{\omega}}^{1s}_{r,j}$ in Eq. (26) and $\Delta\hat{\tilde{\tilde{\omega}}}^{1s}_{r,j}$ in Eq. (27)] and (b) those after adding the O-C terms of the phase observations [$\Delta\tilde{\phi}^{1s}_{r,j}$ in Eq. (29) and $\Delta\tilde{\tilde{\phi}}^{1s}_{r,j}$ in Eq. (30)] of Station WBEE for Satellites G07 and G09 without and with satellite-clock models from 14:00 to 15:00 on March 28, 2017

prediction time point $t_i + t_P$ were set to be equal to those at the last estimation time point t_i, with t_P denoting the prediction time

$$\check{\tilde{\delta}}^{s}_{,j}(t_i + t_P) = \hat{\tilde{\delta}}^{s}_{,j}(t_i) \tag{31}$$

$$\check{\tilde{\iota}}^{s}_{u}(t_i + t_P) = \hat{\tilde{\iota}}^{s}_{u}(t_i) \tag{32}$$

where $\hat{\tilde{\delta}}^{s}_{,j}$ and $\hat{\tilde{\iota}}^{s}_{u}$ = estimated satellite phase biases on GPS L1 and user-specific ionospheric delays for the satellite s, respectively; and $\check{\tilde{\delta}}^{s}_{,j}$ and $\check{\tilde{\iota}}^{s}_{u}$ = predicted satellite phase biases on GPS L1 and user-specific ionospheric delays for the satellite (s), respectively.

The estimable satellite clock (applying satellite-clock model) was predicted with the help of the estimated satellite-clock rate ($\dot{\hat{\tilde{t}}}^{s}$) in the Kalman filter

$$\check{\tilde{dt}}^{s}(t_i + t_P) = \hat{\tilde{dt}}^{s}(t_i) + \dot{\hat{\tilde{t}}}^{s}(t_i) \cdot t_P \tag{33}$$

Alternatively, in case the satellite-clock model is not applied in the network processing, the estimable satellite clock can also be predicted with the help of the postcomputed satellite-clock rates ($\dot{\hat{\tilde{t}}}^{s}$)

$$\check{\tilde{dt}}^{s}(t_i + t_P) = \hat{\tilde{dt}}^{s}(t_i) + \dot{\hat{\tilde{t}}}^{s}(t_i) \cdot t_P \tag{34}$$

The postcomputed satellite-clock rates can be obtained by fitting polynomials using the satellite-clock estimates without clock constraint ($\hat{\tilde{dt}}^{s}$). Assuming that the estimable satellite clock ($\tilde{dt}^{s}$) without a clock model (Fig. 1) behaves similarly to a linear polynomial within a short time span, the polynomial can be fitted with

$$E\left(\tilde{dt}^{s}(t_i)\right) = a^{s}_{0} + a^{s}_{1}(t_i - t_o) \tag{35}$$

where a^{s}_{0} and a^{s}_{1} = offset and rate of estimable clock of satellite (s) at the time point t_i without applying a clock model, respectively; and t_o = starting time of the polynomial fitting. The estimation was performed for all satellites in each epoch, and the estimated parameter $\hat{a}^{s}_{1}$ was used as the satellite-clock rate ($\dot{\hat{\tilde{t}}}^{s}$) in Eq. (34). In this study, the starting time of the polynomial fitting (t_o) was set to be $t_i - 9$ s, which means that the satellite-clock estimates (without clock model) of the last 10 s were used for the polynomial fitting. It is noted that estimating the satellite-clock rates by postcomputing polynomials using the satellite-clock estimates without a clock model violates the assumption that was made for the network Kalman filter. In contrast, the prediction based on the estimated satellite-clock rates applying satellite-clock model [Eq. (33)] directly followed the dynamic model of the satellite clocks in the network Kalman filter.

The predicted combined corrections without ($\check{\tilde{\omega}}^{s}_{u,j}$) and with satellite-clock models ($\check{\tilde{\tilde{\omega}}}^{s}_{u,j}$) were defined as

$$\begin{aligned}\check{\tilde{\omega}}^{s}_{u,j}(t_i + t_P) &= \check{\tilde{dt}}^{s}(t_i + t_P) + \check{\tilde{\delta}}^{s}_{,j}(t_i + t_P) + \mu_j \check{\tilde{\iota}}^{s}_{u}(t_i + t_P),\\ &= \hat{\tilde{dt}}^{s}(t_i) + \dot{\hat{\tilde{t}}}^{s}(t_i) \cdot t_P + \hat{\tilde{\delta}}^{s}_{,j}(t_i) + \mu_j \hat{\tilde{\iota}}^{s}_{u}(t_i),\\ &= \hat{\tilde{\omega}}^{s}_{u,j}(t_i) + \dot{\hat{\tilde{t}}}^{s}(t_i) \cdot t_P\end{aligned} \tag{36}$$

$$\begin{aligned}\check{\tilde{\tilde{\omega}}}^{s}_{u,j}(t_i + t_P) &= \check{\tilde{dt}}^{s}(t_i + t_P) + \check{\tilde{\tilde{\delta}}}^{s}_{,j}(t_i + t_P) + \mu_j \check{\tilde{\iota}}^{s}_{u}(t_i + t_P),\\ &= \hat{\tilde{dt}}^{s}(t_i) + \dot{\hat{\tilde{t}}}^{s}(t_i) \cdot t_P + \hat{\tilde{\delta}}^{s}_{,j}(t_i) + \mu_j \hat{\tilde{\iota}}^{s}_{u}(t_i),\\ &= \hat{\tilde{\tilde{\omega}}}^{s}_{u,j}(t_i) + \dot{\hat{\tilde{t}}}^{s}(t_i) \cdot t_P\end{aligned} \tag{37}$$

where $\hat{\tilde{\omega}}^{s}_{u,j}$ and $\hat{\tilde{\tilde{\omega}}}^{s}_{u,j}$ = estimated user-specific combined network corrections without and with the satellite-clock models, respectively. Fig. 2, shows that the estimable between-satellite-clock rates (applying a satellite-clock model) were equal to the original between-satellite-clock rates

$$\dot{\tilde{dt}}^{1s} = \dot{dt}^{1s} \tag{38}$$

Fig. 9 shows the estimated between-satellite-clock rates without and with clock models for the satellite pair G07 and G09 from 14:00 to 15:00 on March 28, 2017. The line with the legend "no model" represents the between-satellite-clock rates generated by fitting polynomials using the $\hat{\tilde{dt}}^{s}$ of the last 10 s [Eq. (35)]. The line with the legend "IGS" represents the between-satellite-clock rates for the same satellite pair and the same time interval computed using the IGS final satellite clocks (IGS Clock 2017) with a sampling interval of 30 s

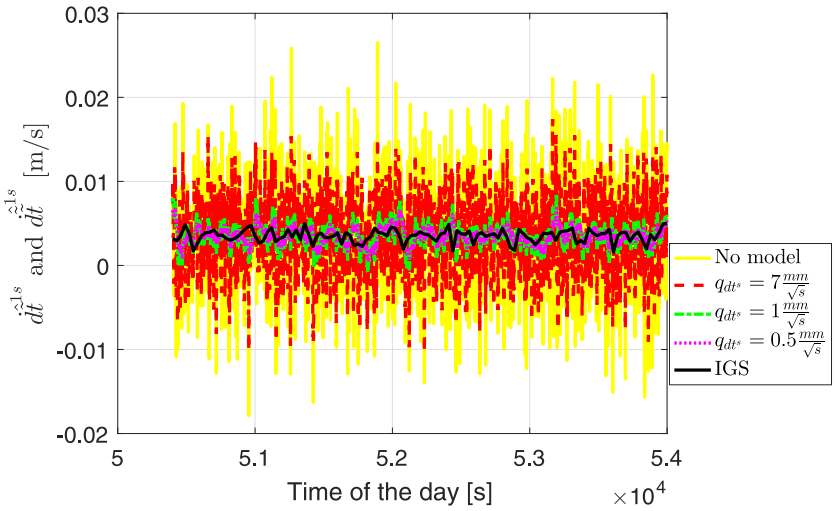

Fig. 9. Estimates of the between-satellite-clock rates for satellites G07 and G09 from 14:00 to 15:00 on March 8, 2017; *no model* represents estimates of between-satellite-clock rates obtained by fitting polynomials [Eq. (35)]; *IGS* represents estimates of between-satellite-clock rates computed using IGS final clock products [Eq. (39)]

$$\dot{\hat{dt}}^{1s}_{\text{IGS}}(t_i) = \dot{\hat{dt}}^{s}_{\text{IGS}}(t_i) - \dot{\hat{dt}}^{1}_{\text{IGS}}(t_i)$$

$$= \frac{\hat{dt}^{s}_{\text{IGS}}(t_{i+1}) - \hat{dt}^{s}_{\text{IGS}}(t_i)}{\Delta t_{i+1}} - \frac{\hat{dt}^{1}_{\text{IGS}}(t_{i+1}) - \hat{dt}^{1}_{\text{IGS}}(t_i)}{\Delta t_{i+1}} \tag{39}$$

where $\hat{dt}^{s}_{\text{IGS}}(t_i)$ = IGS clock bias for satellite (s) at t_i. The time difference (Δt_{i+1}) amounted to 30 s by calculating the IGS between-satellite-clock rates.

Based on the results generated using the IGS satellite clocks (see the line with the legend "IGS" in Fig. 9), the authors assumed that the between-satellite-clock rates for Satellites G07 and G09 from 14:00 to 15:00 on March 28, 2017 varied within millimeters per second. Applying strong satellite-clock constraints helped to reduce the noise in the estimates of the between-satellite-clock rates. The line with the legend "no model," which represents the estimates of the between-satellite-clock rates obtained by fitting polynomials [Eq. (35)], showed the most noisy behaviors among all the different choices. Based on Eq. (20), it can be seen that the between-satellite-clock rates obtained by fitting polynomials ($\dot{\hat{dt}}^{1s}$) included not only the original between-satellite-clock rates ($\dot{dt}^{1s}$), but also the rates of the term $g_1^{1s}\tau_1(t_1)$. However, the rate of the term $g_1^{1s}\tau_1(t_1)$ for the satellite pair G07 and G09 during this time interval varied within tens of micrometers per second. The noisy behavior of the line with the legend "no model" in Fig. 9 was caused by the noisy behavior of the between-satellite-clock estimates without clock constraint (see the solid line in Fig. 6).

For the relevant satellites in the predicted test time intervals, the between-satellite-clock rates computed using the IGS clocks (IGS Clock 2017) all had small amplitudes (from submillimeters per second or even less than millimeters per second). In the case of not applying a satellite-clock model, the authors thus also tested the option to directly set the predicted satellite clocks at $t_i + t_P$ to those at t_i. In other words, apart from obtaining the values of $\dot{\hat{dt}}^{s}$ by fitting polynomials [Eq. (35)], the values of the $\dot{\hat{dt}}^{s}$ can also be directly set to 0 m/s. In the section "Latency and User Positioning Results," for the case without a satellite-clock model, both options (i.e., obtaining the satellite-clock rates by fitting polynomials and directly setting them to 0 m/s) are tested.

Apart from the between-satellite-clock rate, the prediction time (t_P), which varied according to the latency of the network corrections, also influenced the predicted combined corrections [Eqs. (36) and (37)]. The residuals of the predicted between-satellite combined network corrections without ($\Delta\tilde{\tilde{\omega}}^{1s}_{u,j}$) and with satellite-clock models ($\Delta\hat{\tilde{\tilde{\omega}}}^{1s}_{u,j}$) were defined as follows [see also Eq. (28)]:

$$\Delta\tilde{\tilde{\omega}}^{1s}_{u,j}(t_i + t_P) = \tilde{\tilde{\omega}}^{1s}_{u,j}(t_i + t_P) - \hat{p}_1^{1s} \cdot (t_i + t_P - t_0) - \hat{p}_0^{1s} \tag{40}$$

$$\Delta\hat{\tilde{\tilde{\omega}}}^{1s}_{u,j}(t_i + t_P) = \hat{\tilde{\tilde{\omega}}}^{1s}_{u,j}(t_i + t_P) - \hat{p}_1^{1s} \cdot (t_i + t_P - t_0) - \hat{p}_0^{1s} \tag{41}$$

Fig. 10 shows the residuals of the predicted between-satellite combined network corrections without and with applying different satellite-clock constraints with the same prediction time (t_P) of 3 s [Fig. 10(a)] and with a different prediction time (t_P) applying the same clock constraint ($q_{dt^s} = 7$ mm/$\sqrt{\text{s}}$) [Fig. 10(b)] for user station PKVL from 14:00 to 15:00 on March 28, 2017. The line with the legend "no model" in Fig. 10(a) represents the case using $\dot{\hat{dt}}^{s}$ obtained by fitting polynomials [Eq. (35)]. As shown in Fig. 10, the predicted combined corrections were influenced by both the satellite-clock constraint and the prediction time (t_P).

To compare the predicted and estimated network corrections, the differences of the predicted [Eqs. (33) and (34)] and estimated between-satellite clocks without and with satellite-clock models are plotted in Fig. 11(a) for a latency of 3 s, and those for the between-satellite combined network corrections [Eqs. (36) and (37)] are plotted in Fig. 11(b). Without a satellite-clock model (see the lines with the legend "no model" in Fig. 11), the satellite-clock rates were obtained by fitting polynomials [Eq. (35)]. It can be seen that for both the between-satellite clocks and combined network corrections, applying strong satellite-clock models (with q_{dt^s} of 1 and 0.5 mm/$\sqrt{\text{s}}$) helped to reduce the differences between the predictions and the estimations.

Applying a satellite-clock model with a q_{dt^s} of 0.5 mm/$\sqrt{\text{s}}$, Fig. 12 also shows the differences of the predicted and estimated combined network corrections with latencies of 3, 6, and 10 s. The differences were enlarged with increasing latency of the network products.

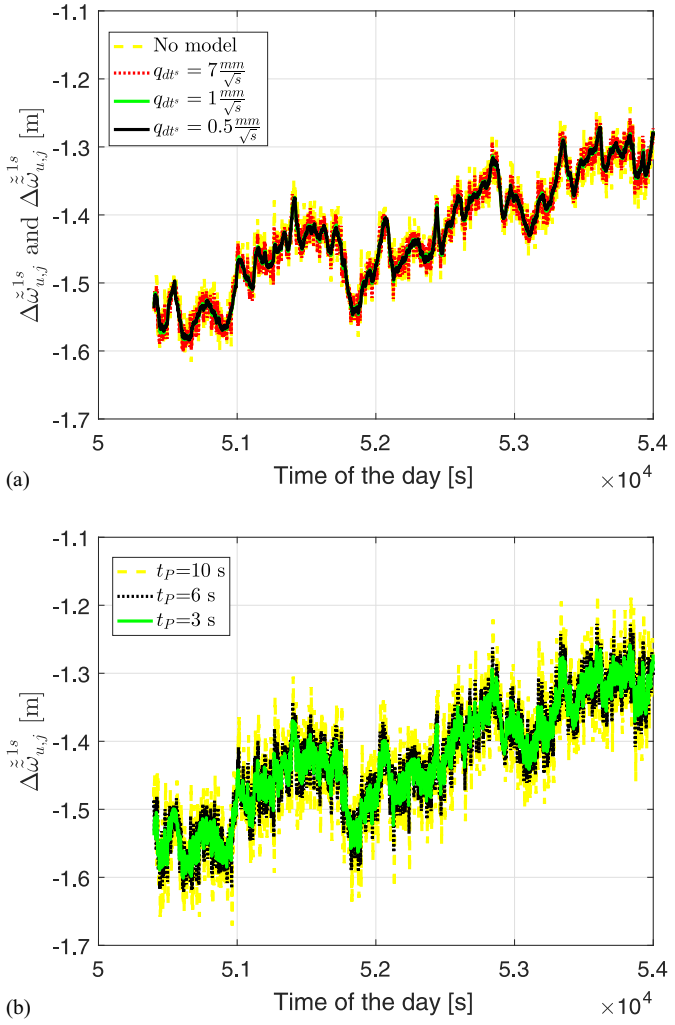

Fig. 10. Residuals of predicted between-satellite combined network corrections [Eqs. (40) and (41)] for user station PKVL and Satellites G07 and G09 from 14:00 to 15:00 on March 28, 2017: (a) without ($\Delta\check{\tilde{\omega}}^{1s}_{u,j}$) and with applying different satellite-clock constraints ($\Delta\check{\tilde{\omega}}^{1s}_{u,j}$) with a prediction time (t_P) of 3 s; (b) applying a satellite-clock model ($\Delta\check{\tilde{\omega}}^{1s}_{u,j}$) of $q_{dt^s} = 7$ mm/$\sqrt{\text{s}}$ with different prediction time

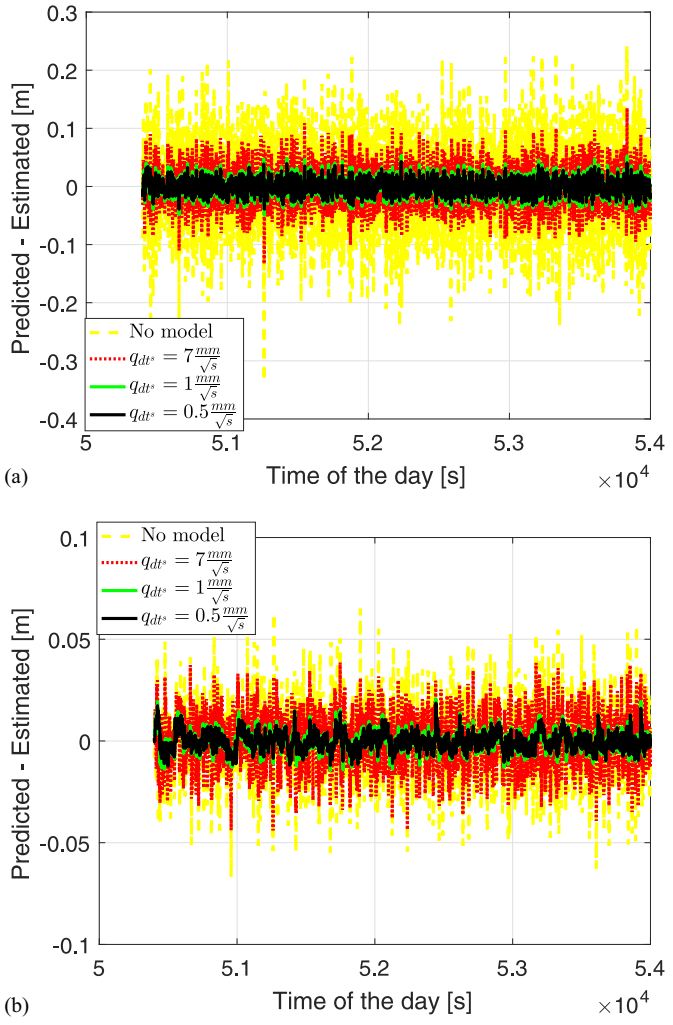

Fig. 11. Differences in (a) predicted and estimated between-satellite clocks [Eqs. (33) and (34)] and (b) predicted and estimated between-satellite combined network corrections [Eqs. (36) and (37)] for G07 and G09 and user station PKVL from 14:00 to 15:00 on March 28, 2017; latency in the case of prediction is 3 s

Latency and User Positioning Results

Because of the time delay of the network products, the estimated satellite clocks, satellite phase biases, and the interpolated user-specific ionospheric delays were predicted with a latency ranging from 3 to 10 s and were provided to the users. For reason of comparison, the authors also computed predictions without a satellite-clock model. The satellite-clock rates can be computed by fitting polynomials using the satellite-clock estimates ($\hat{dt}^s$) without a satellite-clock model of the last 10 s [Eq. (35)]. Because the network corrections were effective or largely effective on a between-satellite level for user positioning with unlinked or weakly linked receiver clocks and hardware biases (Khodabandeh and Teunissen 2015), and based on the fact that the between-satellite-clock rates (obtained using IGS clocks) for the tested time intervals had small amplitudes (submillimeters per second to millimeters per second; see the previous section), the authors also tested the option to directly set the values of the satellite-clock rates [$\dot{\hat{dt}}^s$ in Eq. (34)] to 0 m/s in case no satellite-clock model was applied.

In this study, the station coordinates in the daily final solution provided by GA were used as ground truth (GA 2017). As in the network processing, the zenith-referenced a priori standard deviations of the phase and the code observations were set to 3 mm and 3 dm, respectively. The receiver hardware biases and the ZTDs were time linked with a spectral density of 1 m/$\sqrt{\text{s}}$ and 0.1 mm/$\sqrt{\text{s}}$, respectively. The receiver coordinates were estimated kinematically without a link in time.

Fig. 13 shows the coordinate differences for user station PKVL using the predicted network corrections (with a q_{dt^s} of 0.5 mm/$\sqrt{\text{s}}$ and latencies of 3, 6, and 10 s) and the estimated network corrections in the north, east, and up directions from 14:00 to 15:00 on March 28, 2017. The y-axis was scaled to –5 and 5 cm for the horizontal coordinates, and to –2 and 2 dm for the vertical coordinates. The results were based on partial ambiguity resolution with a predefined success rate of 99.99%. It can be seen that the coordinate differences increased with the increasing latency in all three directions.

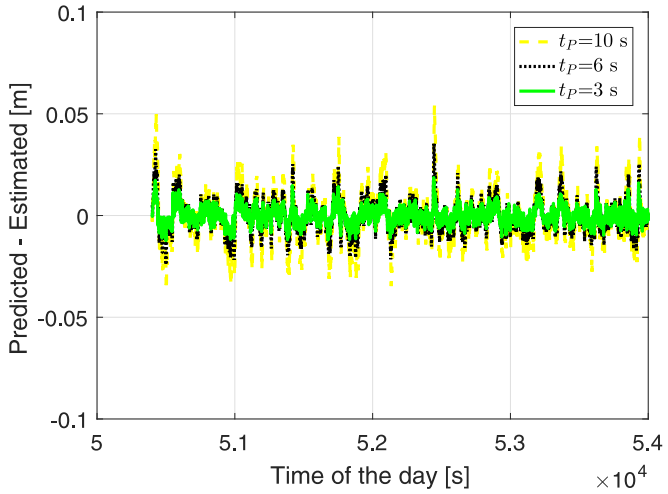

Fig. 12. Differences of the predicted and estimated between-satellite combined network corrections (see Eqs. (36) and (37)) for G07 and G09 and user station PKVL from 14:00 to 15:00 on March 28, 2017 applying satellite-clock model with q_{dt^s} of 0.5 mm/$\sqrt{\text{s}}$ and latencies of 3, 6 and 10 s

To compare the influences of different sets of the predicted network corrections on the user positioning results for different users in different time intervals, the overall root-mean square (RMS) of the coordinate increments was computed using the coordinate increments (with respect to the ground truth) of both user stations from 6:00 to 7:00, from 14:00 to 15:00, and from 22:00 to 23:00 (in GPST) on March 28, 2017 with latencies ranging from 3 to 10 s. The overall RMS is defined as

$$\sigma_x = \sqrt{\frac{\sum_{h=1}^{T}\sum_{u=1}^{U}\sum_{i=N_s}^{N_e} x_{u,h}^2(t_i)}{T \cdot U \cdot (N_e - N_s + 1)}} \tag{42}$$

where T and U = number of tested time intervals and number of user stations, respectively; N_s and N_e = starting and ending time epoch for calculating the RMS of the user positioning results, respectively; and $x_{u,h}(t_i)$ = coordinate increment (with respect to the ground truth) for the user station (u) of the time interval h at time point t_i based on partial ambiguity resolution. The RMS in the north, east, and up directions are denoted as $\hat{\sigma}_N$, $\hat{\sigma}_E$, and $\hat{\sigma}_U$, respectively. The first 10 s were considered as the filter initialization time and were not used for computing the RMS of the coordinates.

Fig. 14 shows the overall RMS of the north, east, and up coordinates applying different prediction methods for different latencies of the network products. The value 0 in the x-axis represents the case without latency (i.e., using the estimated network corrections). "No model ($\dot{\hat{dt}}^s$ =0 m/s)" represents the case where the values of the satellite-clock rate were directly set to 0 m/s, and "no model (polyfit)" represents the case where the satellite-clock rates were computed by fitting polynomials using the satellite-clock estimates without a clock model of the last 10 s [Eq. (35)].

Fig. 14 shows that estimation of satellite-clock rates by fitting polynomials (see the lines with the legend "no model (polyfit)" in Fig. 14) degraded the user positioning results significantly, already by short latencies (e.g., 3 s). Directly setting the values of the satellite-clock rates to 0 m/s avoided the noisy behaviors of the between-satellite-clock rates in Fig. 9. However, the fact that the between-satellite-clock rates were not 0 m/s increased

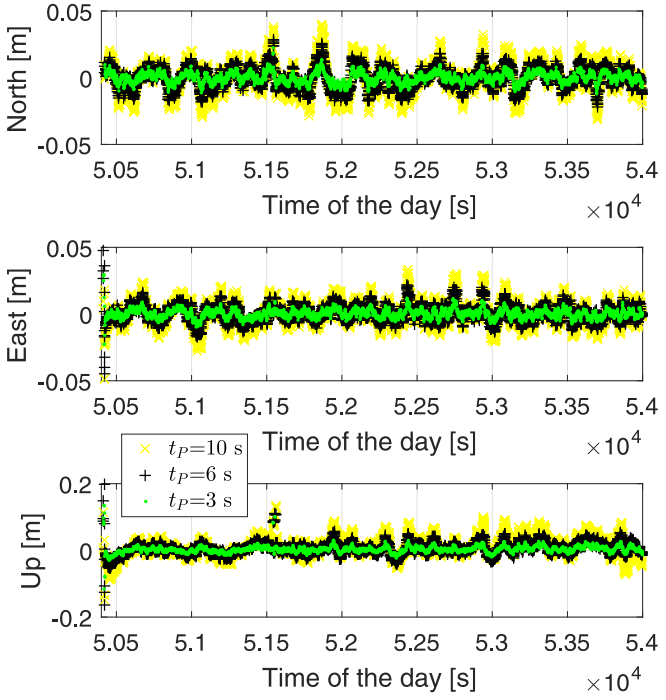

Fig. 13. Coordinate differences for user station PKVL using predicted network corrections (with a q_{dt^s} of 0.5 mm/$\sqrt{\text{s}}$ and latencies of 3, 6, and 10 s) and estimated network corrections in the north, east, and up directions from 14:00 to 15:00 on March 28, 2017

the biases in the predicted between-satellite combined network corrections with the increasing latencies. For long latencies (e.g., larger than 8 s), large degradation in the user positioning results can thus occur. Using the satellite-clock rates with weak satellite-clock models (i.e., with q_{dt^s} = 7 mm/$\sqrt{\text{s}}$) did not generate better results compared to the case where the $\dot{\hat{dt}}^s$ was directly set to 0 m/s, especially in the vertical direction. However, by strengthening the constraint in the satellite-clock model, the noise in the between-satellite-clock rates was significantly reduced (see the lines with q_{dt^s} of 1 and 0.5 mm/$\sqrt{\text{s}}$ in Fig. 9). This led to improvements in all three directions of the user positioning results (see the lines with q_{dt^s} of 1 and 0.5 mm/$\sqrt{\text{s}}$ in Fig. 14). Compared to the cases without a satellite-clock model, the benefits were especially large for long latencies with t_P larger than 8 s. Applying strong satellite-clock constraint (i.e., with a q_{dt^s} of 0.5 or 1 mm/$\sqrt{\text{s}}$), the RMS of the coordinates were reduced to centimeters in the horizontal directions and decimeters in the vertical direction for a latency larger than 6 s compared to the cases without satellite-clock model.

Conclusion

This contribution studied the estimability of the parameters applying a dynamic satellite-clock model in the PPP-RTK network processing under a single-frequency and ionosphere-weighted scenario. With dynamic satellite-clock models incorporated in the network Kalman filter, the authors developed a single-frequency network full-rank model applicable to an arbitrary GNSS. To test the implementation of the satellite-clock model, real data from a small-scale network in three different time intervals were used to compute the estimated and the predicted network corrections (the estimable satellite clocks, satellite phase biases, and ionospheric delays). The

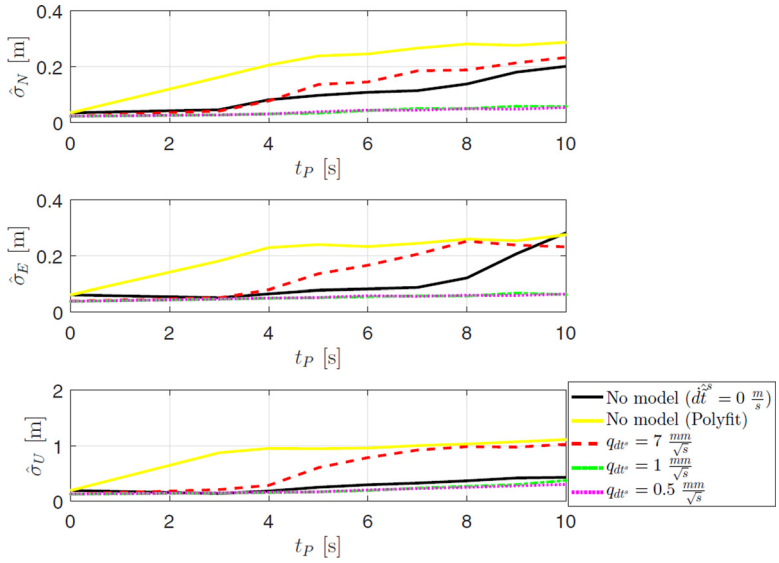

Fig. 14. Overall RMS of the north, east, and up coordinate increments (with respect to the ground truth) using the estimated and predicted network corrections from 6:00 to 7:00, 14:00 to 15:00, and 22:00 to 23:00 (in GPST) on March 28, 2017 with latencies ranging from 3 to 10 s based on partial ambiguity resolution

estimated and predicted network corrections were provided to the users, and the influences of the satellite-clock models on the user positioning results were studied and discussed with respect to their RMS (deviated from the ground truth) for latencies ranging from 3 to 10 s. Predictions without satellite-clock models were also performed for reason of comparison.

In this study, it was found that the estimated combined network corrections did not benefit much from satellite-clock models. However, modeling satellite clocks was shown to be beneficial to reduce the noise in the *predicted* between-satellite combined network corrections in the case of latencies of the network products. These improvements were also reflected in the user positioning results. Without a satellite-clock model, the results were computed both by directly setting the values of the satellite-clock rates to 0 m/s and by fitting polynomials using the satellite-clock estimates without constraint of the last 10 s. The latter case already generated decimeter-level RMS in all three directions at a short latency of 3 s. Directly setting the values of the satellite-clock rates to 0 m/s also led to decimeter-level RMS in all three directions at a long latency larger than 8 s. Applying a strong satellite-clock model for GPS satellites with, for example, q_{dt^s} equal to 0.5 or 1 mm$/\sqrt{\text{s}}$, the RMS of the user coordinates were reduced to centimeters in the horizontal directions and decimeters in the vertical direction for latencies larger than 6 s. Compared to the discussed prediction methods without a satellite-clock model, advantages of the strong satellite-clock models in single-frequency PPP-RTK network processing were directly reflected in user positioning results, especially in cases of long latencies of the network products.

Acknowledgments

The authors thank the IGS, GA, and Vicmap Position—GPSnet (Victoria State Government) for providing the orbit and the clock products, the precise coordinates, and the observation data of the stations. The orbit and clock products were obtained through the online archives of the Crustal Dynamics Data Information System (CDDIS), NASA Goddard Space Flight Center, Greenbelt, MD (ftp://cddis.gsfc.nasa.gov/gnss/products/). The authors also thank their colleagues in the GNSS Research Centre, Curtin University, for their contributions on the development of the Curtin PPP-RTK Software. P. J. G. Teunissen is recipient of an Australian Research Council (ARC) Federation Fellowship (Project FF0883188).

References

Allan, D. W. (1987). "Time and frequency (time-domain) characterization, estimation, and prediction of precision clocks and oscillators." *IEEE T. Ultrason. Ferroelectr. Freq. Control*, 34(6), 647–654.

Baarda, W. (1981). *S-transformations and criterion matrices*. Vol. 5(1) of *Publications on Geodesy*, 2nd Rev. Ed. Netherlands Geodetic Commission, Delft, Netherlands.

Banville, S., Collins, P., Zhang, W., and Langley, R. B. (2014). "Global and regional ionospheric corrections for faster PPP convergence." *Navigation*, 61(2), 115–124.

Bevis, M., Businger, S., Herring, T., Rocken, C., Anthes, R., and Ware, R. (1992). "GPS meteorology: Sensing of atmospheric water vapor using the Global Positioning System." *J. Geophys. Res.*, 97(D14), 15787–15801.

Collins, P. (2008). "Isolating and estimating undifferenced GPS integer ambiguities." *Proc., 2008 National Technical Meeting of the Institute of Navigation*, Institute of Navigation, Manassas, VA, 720–732.

Dach, R., Hugentobler, U., Fridez, P., and Meindl, M. (2007). *Bernese GNSS software version 5.0. User manual*, Astronomical Institute, Univ. of Bern, Bern, Switzerland.

Dow, J. M., Neilan, R. E., and Rizos, C. (2009). "The International GNSS service in a changing landscape of global navigation satellite systems." *J. Geod.*, 83(3–4), 191–198.

Eueler, H. J., and Goad, C. C. (1991). "On optimal filtering of GPS dual frequency observations without using orbit information." *Bull. Geod.* 65(2), 130–143.

GA (Geoscience Australia). (2017). "Daily SINEX files". ⟨ftp://ftp.ga.gov.au/geodesy-outgoing/gnss/solutions/final/⟩ (May 2017).

Ge, M., Gendt, G., Rothacher, M., Shi, C., and Liu, J. (2008). "Resolution of GPS carrier-phase ambiguities in precise point positioning (PPP) with daily observations." *J. Geod.*, 82(7), 389–399.

Geng, J., Teferle, F. N., Meng, X., and Dodson, A. H. (2011). "Towards PPP-RTK: Ambiguity resolution in real-time precise point positioning." *Adv. Space Res.*, 47(10), 1664–1673.

Google Earth. (2017). "Google earth imagery." (October 18, 2017). Google earth 7.0.3.8542. Victoria, Australia. 37° 47′13.50″S, 144° 58′57.07″E,

Eye alt 66.19 km. TerraMetrics 2017. DigitalGlobe 2017. ⟨https://www.google.com/earth/⟩ (December 2017).
Hauschild, A., and Montenbruck, O. (2009). "Kalman-filter-based GPS clock estimation for near real-time positioning." *GPS Solut.*, 13(3), 173–182.
Hofmann-Wellenhof, B., Lichtenegger, H., and Wasle, E. (2008). *GNSS—Global navigation satellite systems: GPS, GLONASS, Galileo, and more*, Springer-Verlag, Wien, Austria.
Huisman, L., Teunissen, P. J. G., and Hu, C. (2012). "GNSS precise point positioning in regional reference frames using real-time broadcast corrections." *J. Appl. Geod.*, 6(1), 15–23.
IGS (International GNSS Service) Clock. (2017). "International GNSS Service, GNSS final combined satellite and receiver clock solution (30 second) product." NASA Crustal Dynamics Data Information System, Greenbelt, MD ⟨ftp://cddis.gsfc.nasa.gov/⟩ (June 2017).
Khodabandeh, A., and Teunissen, P. J. G. (2015). "An analytical study of PPP-RTK corrections: Precision, correlation and user-impact." *J. Geod.*, 89(11), 1109–1132.
Laurichesse, D., and Mercier, F. (2007). "Integer ambiguity resolution on undifferenced GPS phase measurements and its application to PPP." *Proc., ION GNSS 2007*, Institute of Navigation, Manassas, VA, 839–848.
Laurichesse, D., Mercier, F., and Berthias, J. P. (2010). "Real-time PPP with undifferenced integer ambiguity resolution, experimental results." *Proc., ION GNSS 2010*, Institute of Navigation, Manassas, VA, 2534–2544.
Leandro, R., et al. (2011). "RTX positioning: The next generation of cm-accurate real-time GNSS positioning." *Proc., ION GNSS 2011*, Institute of Navigation, Manassas, VA, 1460–1475.
Li, W., Nadarajah, N., Teunissen, P. J. G., Khodabandeh, A., and Chai, Y. (2017). "Array-aided single-frequency state-space RTK with combined GPS, Galileo, IRNSS, and QZSS L5/E5a observations." *J. Surv. Eng.*, 10.1061/(ASCE)SU.1943-5428.0000227, 04017006.
Loyer, S., Perosanz, F., Mercier, F., Capdeville, H., and Marty, J. C. (2012). "Zero-difference GPS ambiguity resolution at CNES-CLS IGS analysis center." *J. Geod.*, 86(11), 991–1003.
Odijk, D. (2002). "Fast precise GPS positioning in the presence of ionospheric delays." Ph.D. thesis, Delft Univ. of Technology ⟨https://repository.tudelft.nl/islandora/object/uuid:40d49779-2ef4-4641-9ae4-f591871063fa?collection=research⟩ (December 2017).
Odijk, D., et al. (2017). "PPP-RTK by means of S-system theory: Australian network and user demonstration." J. Spat. Sci., 62(1), 3–27.
Odijk, D., Arora, B. S., and Teunissen, P. J. G. (2014a). "Predicting the success rate of long-baseline GPS+Galileo (partial) ambiguity resolution." *J. Navig.*, 67(3), 385–401.
Odijk, D., Teunissen, P. J. G., and Huisman, L. (2012a). "First results of mixed GPS-GIOVE single-frequency RTK in Australia." *J. Spat. Sci.*, 57(1), 3–18.
Odijk, D., Teunissen, P. J. G., and Khodabandeh, A. (2014b). "Single-frequency PPP-RTK: Theory and experimental results." *Earth on the edge: Science for a sustainable planet. IAG symposia*, Vol. 139, C. Rizos and P. Willis, eds., Springer, Berlin, Heidelberg, 571–578.
Odijk, D., Teunissen, P. J. G., and Zhang, B. (2012b). "Single-frequency integer ambiguity resolution enabled GPS precise point positioning." *J. Surv. Eng.*, 10.1061/(ASCE)SU.1943-5428.0000085, 193–202.
Odolinski, R., and Teunissen, P. J. G. (2017). "Low-cost, high-precision, single-frequency GPS-BDS RTK positioning." *GPS Solut.*, 21(3), 1315–1330.
Riley, W. J. (2008). *Handbook of frequency stability analysis.* NIST Special Publication 1065, U.S. Government Printing Office, Washington, DC.
Saastamoinen, J. (1972). "Contribution to the theory of atmospheric refraction." *Bull. Geod.*, 105(1), 279–298.
Senior, K. L., Ray, J. R., and Beard, R. L. (2008). "Characterization of periodic variations in the GPS satellite clocks." *GPS Solut.*, 12(3), 211–225.
Springer, T. A., and Hugentobler, U. (2001). "IGS ultra rapid products for (near-) real-time applications." *Phys. Chem. Earth, Part A.*, 26(6–8), 623–628.
Teunissen, P. J. G. (1985). "Zero order design: Generalized inverses, adjustment, the datum problem and S-transformations." *Optimization and design of geodetic networks*, E. W. Grafarend and F. Sansò, eds., Springer, Berlin, Heidelberg, 11–55.
Teunissen, P. J. G., and Khodabandeh, A. (2015). "Review and principles of PPP-RTK methods." *J. Geod.*, 89(3), 217–240.
Teunissen, P. J. G., and Montenbruck, O. (2017). *Springer handbook of global navigation satellite systems*, Springer International Publishing, Cham, Switzerland.
Teunissen, P. J. G., Odijk, D., and Zhang, B. (2010). "PPP-RTK: Results of CORS network-based PPP with integer ambiguity resolution." *J. Aeronaut., Astronaut. Aviation, Ser. A*, 42(4), 223–230.
van Bree, R. J. P., and Tiberius, C. C. J. M. (2012). "Real-time single-frequency precise point positioning: Accuracy assessment." *GPS Solut.*, 16(2), 259–266.
van Dierendonck, A. J., McGraw, J. B., and Brown, R. G. (1984). "Relationship between Allan variances and Kalman filter parameters." *Proc., PTTI 1984*, NASA Goddard Space Flight Center, Greenbelt, MD, 273–293.
Wang, K., Khodabandeh, A., and Teunissen, P. J. G. (2017). "A study on predicting network corrections in PPP-RTK processing." *Adv. Space Res.*, 60(7), 1463–1477.
Wübbena, G., Schmitz, M., and Bagge, A. (2005). "PPP-RTK: Precise point positioning using state-space representation in RTK networks." *Proc., ION GNSS 2005*, Institute of Navigation, Manassas, VA, 2584–2594.
Younes, S. A. M. (2016). "Modeling investigation of wet tropospheric delay error and precipitable water vapor content in Egypt." *Egypt. J. Remote Sens. Space Sci.*, 19(2), 333–342.
Yu, X., and Gao, J. (2017). "Kinematic precise point positioning using multi-constellation global navigation satellite system (GNSS) observations." *ISPRS Int. J. Geo-Inf.*, 6(1), 6.